

# Diag2Diag: Multimodal super-resolution diagnostics for physics discovery with application to fusion

Azarakhsh Jalalvand<sup>1\*</sup>, Max Curie<sup>1</sup>, SangKyeun Kim<sup>2</sup>,  
Peter Steiner<sup>1</sup>, Jaemin Seo<sup>3</sup>, Qiming Hu<sup>2</sup>,  
Andrew Oakleigh Nelson<sup>4</sup>, Egemen Kolemen<sup>1,2\*</sup>

<sup>1\*</sup>Department of Mechanical and Aerospace Engineering, Princeton University, Olden Street, Princeton, 08540, NJ, USA.

<sup>2</sup>Princeton Plasma Physics Laboratory, Stellarator Road, Princeton, 08543, NJ, USA.

<sup>3</sup>Department of Physics, Chung-Ang University, Seoul, South Korea.

<sup>4</sup>Applied Physics and Applied Mathematics, Columbia University, W. 120th Street, New York, 10027, NY, USA.

\*Corresponding author(s). E-mail(s): [azarakhsh.jalalvand@princeton.edu](mailto:azarakhsh.jalalvand@princeton.edu); [ekolemen@princeton.edu](mailto:ekolemen@princeton.edu);

## Abstract

This paper introduces a groundbreaking multimodal neural network model designed for resolution enhancement, which innovatively leverages inter-diagnostic correlations within a system. Traditional approaches have primarily focused on unimodal enhancement strategies, such as pixel-based image enhancement or heuristic signal interpolation. In contrast, our model employs a novel methodology by harnessing the diagnostic relationships within the physics of fusion plasma. Initially, we establish the correlation among diagnostics within the tokamak. Subsequently, we utilize these correlations to substantially enhance the temporal resolution of the Thomson Scattering (TS) diagnostic, which assesses plasma density and temperature. This enhancement goes beyond simple interpolation, offering a super resolution that preserves the underlying physics inherent in inter-diagnostic correlation. Increasing the resolution of TS from conventional 0.2 kHz to 500 kHz could show the diagnostic capability of capturing the structural evolution of plasma instabilities and the response to external field perturbations, that were challenging with conventional diagnostics. This physics-preserving super-resolution technique

may enable the discovery of new physics that were previously undetectable due to resolution limitations, or allow for the experimental verification of phenomena that had only been predicted through computationally intensive simulations.

**Keywords:** Diagnostics, Machine Learning, Fusion pilot plant, Synthetic Diagnostic

## 1 Introduction

The success of nuclear fusion for energy production strongly depends on monitoring and manipulating the plasma condition to achieve the highest performance while avoiding unstable regimes. It was recently shown that [Artificial Intelligence \(AI\)](#) can be a helpful tool to achieve that goal [1–4]. The experimental fusion reactors such as DIII-D [5] make use of a variety of diagnostics for effective plasma monitoring and control [6]. The different diagnostics form a complementary set for extracting as much information from the plasma as possible. For example, the [Electron Cyclotron Emission \(ECE\)](#) diagnostic system measures electron temperature [7], [CO<sub>2</sub> interferometer \(Interferometer\)](#) measures electron density and its fluctuations [8], [Motional Stark Effect \(MSE\)](#) measures the magnetic field [9], and [Thomson Scattering \(TS\)](#) measures the electron temperature and density [10]. These measurements each capture different physical information from the plasma. Although it is likely that there exists some kind of correlation or coupling between the different diagnostics, the exact relationship cannot be specified analytically. [Machine Learning \(ML\)](#) can be an interesting candidate for identifying hidden relationships in data. Learning the hidden relationships among different diagnostics would be a great asset to enhance their measurements, and it also helps to find a minimal set of diagnostics for a future reactor in which the availability of diagnostics is limited due to the cost and hardware constraints.

One of the most critical issues for fusion reactors is the [Edge Localized Mode \(ELM\)](#), an instability that occurs at the plasma edge under high-confinement conditions. This edge instability delivers transient and intense heat flux outward, which can cause irreversible damage to the wall in a reactor-scale device. Therefore, understanding and controlling this phenomenon is a major challenge that must be resolved [2, 11]. However, the detailed physical mechanism of [ELMs](#) and structural response to the external field occurring within milliseconds are still subjects of ongoing debate. High-frequency diagnostics like [ECE](#) and [Interferometer](#) possess sufficient time resolution to observe these fast dynamics, but their limited spatial resolution and measurement conditions pose challenges in clearly observing the structural characteristics of [ELMs](#). On the other hand, [TS](#) offers high spatial resolution capable of observing detailed structures, but its temporal resolution is too low to elucidate the exact mechanism of [ELMs](#). To address these limitations of [TS](#), we hypothesize that a data-driven model with a multimodal input comprising the high-frequency diagnostics can effectively make use of internal correlations in order to estimate [TS](#). This enhances the temporal resolution of the existing [TS](#) diagnostics without upgrading hardwares, enabling a so-called **super-resolution TS** diagnostics, as a tool for deeper physical analysis of plasma behavior.

Various fields have developed ML-based spatial or temporal super-resolution techniques, but these mostly involve upsampling through linear or nonlinear interpolation of the given information. These are applicable only to regularly sampled data and are challenging to generate finer-scale phenomena undetectable at the time resolution of the target sensor (which will be compared in more detail in Section 6.6). Our work goes beyond plausible interpolation; it is a physics-preserving super-resolution to reconstruct events missed by target diagnostics, by learning the correlation between different diagnostics, which is, to our best knowledge, the first attempt of its kind.

More specifically, we train a Neural Network (NN) on aligned samples from Interferometer, ECE, MSE, Magnetic probes (Magnetics), Charge Exchange Recombination (CER) as input to estimate TS diagnostic. Later, we use the trained NN model to generate additional TS samples with a high temporal resolution. We evaluate this model in several ways:

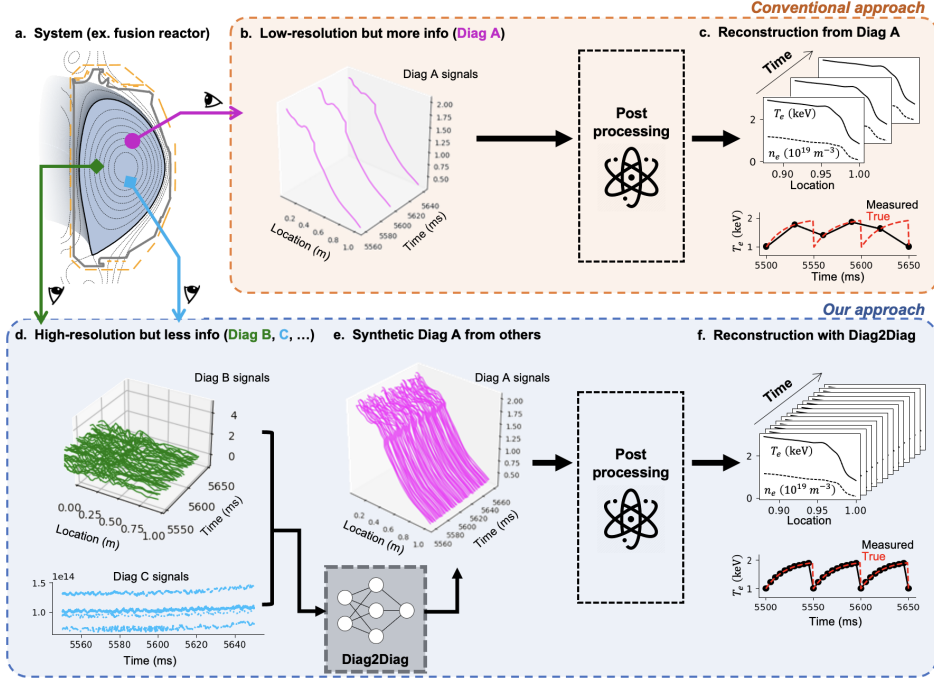
- First of all, we show that we can generate one diagnostic from another, particularly Interferometer from ECE, since there must exist intrinsic correlations between these diagnostics, although they cannot be described analytically. We compare the original and generated Interferometer spectrograms based on similarity scores and based on the task of Alfvén Eigenmode (AE) detection with the model [12].
- Next, we train a model to generate TS signals from CER, Interferometer, ECE, Magnetics and MSE signals. We again compare the original and generated TS diagnostics based on similarity scores.
- In a final step, we use the trained TS generation model for a super-resolution TS diagnostic and present its capability for investigating the ELM cycles [13] and the mechanism of Resonant Magnetic Perturbation (RMP) effect on the pedestal degradation [14].

Figure 1 summarizes the main methodology for this work. DIII-D utilizes hundreds of diagnostics for monitoring the plasma. These diagnostics have different temporal resolutions. A potential ML model can learn the intrinsic correlations among diagnostics and thus generate one from others. This works for both, time-series and spectrograms, although different variants of NN are used. The design choices and the optimization and training strategies are described in the following sections.

## 2 ML-based mapping between different diagnostics

For developing an ML-based super-resolution TS diagnostic from other diagnostics, it is essential to verify the existence, strength, and robustness of correlation among them. We therefore approach this in several steps as described subsequently.

The aim of the first step is to show that we can estimate the spectrograms of one diagnostic based on another. As was discussed in Section 1, it is very likely that different diagnostics have intrinsic correlations. For example, based on thermodynamics there should be a correlation between electron temperature, which is measured by ECE, and density fluctuations measured by Interferometer. We now show that a NN is able to learn exactly this relationship by mapping from ECE spectrograms to Interferometer spectrograms as illustrated in Figure 2.



**Fig. 1:** Main methodology. (a) The configuration of diagnostics in the system. (b) The low temporal resolution diagnostics. (c) Low resolution profile extracted from the diagnostic. (d) High temporal resolution diagnostics. (e) Synthetic super resolution diagnostics generated using Diag2Diag. (f) High resolution profile extracted from the synthetic diagnostic.

Figures 2(b) and (d) show example spectrograms obtained from the raw signals of [ECE](#) and [Interferometer](#), respectively, whose measurement positions and paths can be seen in Figure 2(a). We designed and trained a [Convolutional Neural Network \(CNN\)](#) that takes 40 [ECE](#) spectrograms as input and reconstructs 4 target [Interferometer](#) spectrograms. The detailed settings for calculating spectrograms from raw signals and training the [CNN](#) can be found in Sections 6.3 and 6.4. The reconstructed synthetic [Interferometer](#) spectrograms, shown in Figure 2(c), visually confirm the plausible reconstruction of features such as frequency chirping and harmonics seen in the original 2(d).

Besides the image comparison, we are also interested in studying how much of the underlying physics information is preserved using this method. Therefore we evaluate the trained model on the downstream task of the [AE](#) detection. Based on the reconstructed and the measured [Interferometer](#) spectrograms, we use the model proposed in [12] to detect [AE](#). From Figure 2, we can visually observe that the [CNN](#) model was able to reconstruct the pronounced coherent activities in the spectrogram, and the Toroidal [AE](#) (TAE) scores also show that there is enough information in

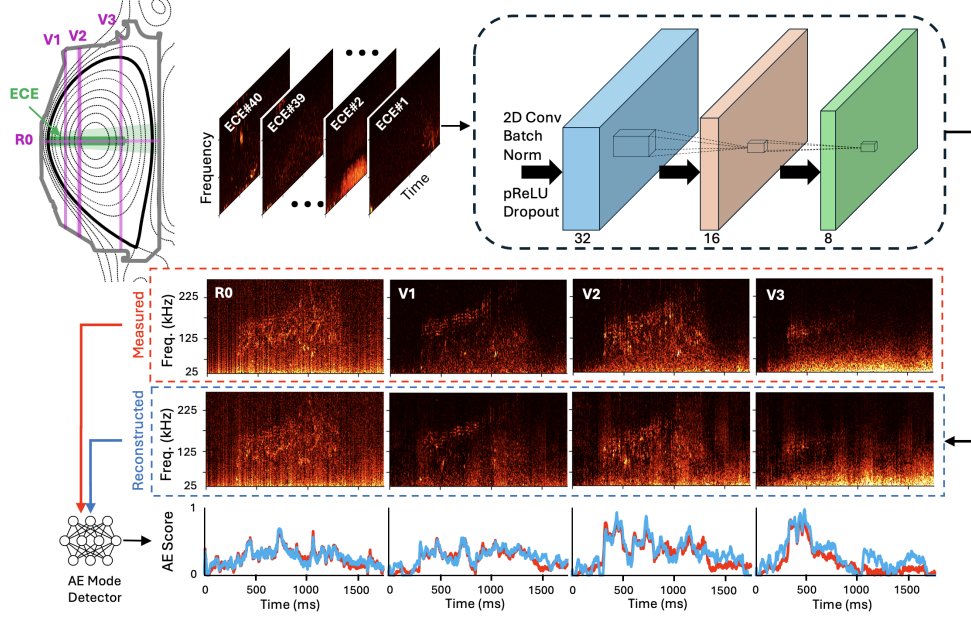


**Fig. 2:** Mapping between spectrograms from different diagnostics. ECE spectrograms form a 40-channel tensor as the input to the CNN. The outputs are the four channels of Interferometer spectrograms.

the reconstructed spectrogram to detect the AE mode after applying the predefined threshold [12].

This result supports that using ML can extract the intrinsic correlation amongst diagnostics. We can now go one step further and face the generation of TS signals from other diagnostics based on raw time-series.

### 3 Multimodal super-resolution diagnostic

In the previous section, we showed the capability of data-driven models in learning the correlation among different diagnostics, by showing that the coherent and physically meaningful patterns in a spectrogram can be reconstructed from other diagnostics. In this section, we switch from spectrograms to time-series signals and show that the amplitude of a diagnostics can be reconstructed from other diagnostics. More importantly, we will show that if the input diagnostics are of much higher temporal resolution compared to the target one, such a model can be used to increase the time resolution of the target signals in a much more intelligent way compared to the conventional uni-modal interpolations. As a use case, we target TS, one of the most important diagnostics that measure the density and pressure profile of plasma. However as mentioned earlier, its low sampling rate (200 Hz) is a bottleneck in studying the plasma evolution in the rapidly changing events such as ELM.

We consider a suite of input diagnostics including [Interferometer](#), [ECE](#), [Magnetics](#), [CER](#), and [MSE](#) with sampling rates of 1.66 MHz, 500 kHz, 200 kHz, 200 Hz, and 4 kHz, respectively.

To obtain a dataset suitable for this task, all the included diagnostics are aligned with the [TS](#) sampling time steps by matching their most recent measured sample. In this way, we create a dataset with which we train the neural network for this task. Since the sampling steps of [TS](#) are not uniform (See [Figure 3](#)), we did not use a conventional [NN](#) for time-series data analysis such as recurrent neural network. Instead, we opted for memory-less models, namely [Multilayer Perceptron \(MLP\)](#). However, we included the first and second derivatives of the high-resolution input diagnostics, [ECE](#) and [Interferometer](#), to include the temporal evolution information.

[Figure 3\(a\)](#) shows synthetic [TS](#) signals (in red) reconstructed through the trained [MLP](#) model ([Diag2Diag](#)) from other high-frequency diagnostics, where the original [TS](#) signals are also shown with black asterisks. We can observe that the synthetic signals closely follow the original signals. Furthermore, while the original signals almost fail to capture [ELM](#) events (identifiable by the gray  $D_\alpha$  signals), the synthetic signals accurately capture the events missed between the original signals. This now enables precise analysis for new discoveries that could not be performed with the existing low-resolution [TS](#) diagnostics, which will be discussed in [Section 4](#).

## 4 Science discovery

In what follows, we investigate whether the synthetic super-resolution diagnostics can help to verify the hypotheses in fusion plasma physics that have been proposed theoretically, or by simulations, but have never been visualized with the experimental data due to the lack of diagnostic resolution. In the following subsections we study two phenomena namely, the [ELM](#) cycle analysis and the mechanism of plasma response to [RMP](#) modulation.

### 4.1 Case 1: Investigating ELM cycles in DIII-D

To mitigate the absence of effective high temporal resolution diagnostics to study fast activities, an option would be to set up the system to repeat that activity with as identical characteristics as possible several times. As long as the sampling time and the activity's temporal evolution are not synchronized perfectly, by collecting and aggregating the measurements of the several activity occurrences, we can hope to have better overview of the whole activity cycle. [Fig. 3\(b\)](#) illustrates an example of this approach in which an activity has been repeated three consecutive times and diagnosed by a low temporal resolution sensor. While it is difficult to observe the pattern of the whole cycle from each occurrence, the aggregated observation reveals the cycle nicely. Such an approach was adopted previously to investigate the [ELM](#) cycle in DIII-D [[13](#)].

As presented in [Fig. 3\(c\)](#), in DIII-D discharge 174823 [[13](#)], there are over 20 highly similar repeated cycles of energy growth ending in explosive bursts ([ELMs](#)). This activity modifies the electron temperature in highly regular manner, leading to growth and decay with a period around 100 ms.

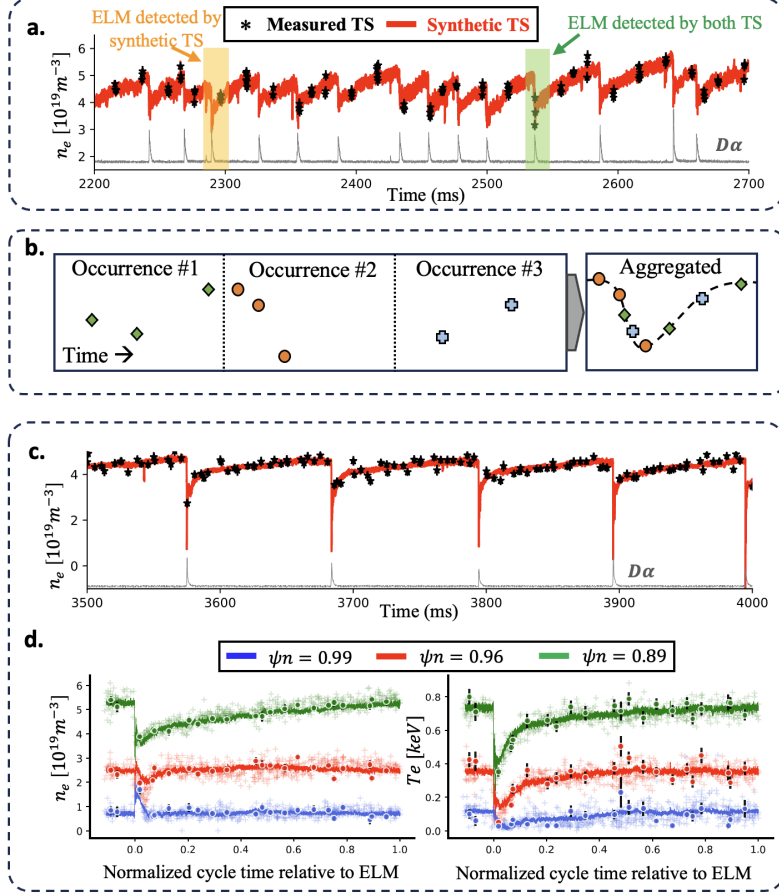


**Fig. 3:** (a) Comparison of the electron density by the original TS and the synthetic TS generated by Diag2Diag, for the DIII-D shot 153674.  $D_\alpha$  with arbitrary units is plotted as an indicator of ELMs. An example of ELM event detected by both diagnostics, and another example only detected by synthetic TS are highlighted in green and orange, respectively. (b) Illustration of aggregating the low temporal resolution measurement for repetitive occurrences of a fast transient activity to provide a better overview of the activity's evolution cycle. (c) Comparison of the electron density by the original TS and the synthetic TS generated by Diag2Diag, for the DIII-D shot 174823. (d) The transparent crosses show aggregating the measured TS for many ELM cycles of the DIII-D shot 174832. The circle highlights the measures TS for one selected ELM cycle and the solid lines present the super-resolution TS which agreeably match the measures TS.  $t = 0$  represents the time when ELM is identified by  $D_\alpha$ .

Interestingly, the extremely regular and slow nature of the ELMs in this discharge, which is relatively rare in tokamak plasmas, allows experimental investigation into the inter-ELM dynamics of the electron temperature and density that would otherwise



be impossible with TS diagnostics. The highly reproducible nature of ELM activity enables an overlay of all the cycles on top of each other by aligning the ELM events like Fig. 3(b). By overlaying the accumulated TS measurements in this manner, the dynamics of ELM cycle is revealed for electron temperature and density, as shown in Fig. 3(d) with transparent crosses for three difference spatial locations. Here, we also presented the TS measurements for a single cycle with solid dots. Notably, the ELM events themselves present a rapid pressure decrease that can hardly be captured with the slow sampling rate of TS.

The super-resolution TS enables us to have a high temporal resolution of  $n_e$  and  $T_e$  as shown in Fig. 3(d) for that selected ELM cycle with solid lines. The super-resolution TS presents a similar trend to the aggregated TS, while it also matches nicely with the single period TS measurements (dots). This plot showcases the ability of super-resolution TS to capture the dynamics of the plasma with high accuracy.

In more general plasmas, the ELMs are more irregular, faster and harder to define, preventing robust inter-ELM profile analysis with TS. This can already be observed in our other test discharge 153674, as shown in Fig. 3(a) which show the TS measurements during several ELM cycles. Interestingly even in such rapid ELM cycles, the super resolution TS capture almost all the ELMs as indicated by  $D_\alpha$ , while it also nicely matches the measurements wherever available.

This exercise shows that super-resolution TS tracks beautifully with aggregated TS which can be used as the ground truth. The measured TS for the shown ELM cycle almost sits on top of the super-resolution TS shows that the TS not only provides the information of repeated trends, but also the dynamics of the electron that is unique to each cycle.

## 4.2 Case 2: Unveiling diagnostic evidence of RMP mechanism on the plasma boundary

One promising strategy to suppress ELMs is employing RMPs [15] generated by external 3D field coils. The typical setup of external coils encircling the plasma is depicted in Fig. 4(a). These fields effectively reduce the temperature and density at the confinement pedestal, stabilizing the energy bursts in the edge region. This stabilization is crucial as it actively reduces the intense, bursty damage to the wall and mitigates seed perturbations that could drive additional core instabilities. Consequently, International Thermonuclear Experimental Reactor (ITER) relies on RMPs to maintain a burst-free burning plasma in a tokamak. However, the detailed mechanism of pedestal degradation by RMPs still remains a challenge. Because the understanding of this physics is vital for the robust projection of the RMP effect on future devices, it needs urgent exploration.

The leading theory [16–18] for explaining the reduced pedestal by RMPs is the formation of magnetic islands by an external 3D field. As illustrated in Figure 4(a), RMPs can create these magnetic islands on resonant magnetic surfaces. These islands promote strong radial transport and flatten the local gradients near the island, significantly degrading the density and temperature profiles. Recent modeling efforts [16, 19, 20] have shown that these magnetic islands can form both at the top and the foot of the pedestal, contributing to the observed degradation of temperature and density profiles. This model has successfully replicated the experimentally observed



pedestal degradation, demonstrating good quantitative accuracy and reinforcing its role as a promising mechanism for RMP-induced pedestal degradation. However, this theory has not yet been fully substantiated, as there is no evidence to confirm the flattening of profiles at islands, which is central to the proposed mechanism. This is due to the spatially narrow island width (expected from theory), the oscillatory behavior of plasma boundary, and source evolution, which makes diagnostics analysis difficult. Here, measuring the perturbative time evolution of the profile by the modulation in RMP amplitude can be an effective way to overcome these difficulties to prove the island effect. However, this was limited due to the insufficient time resolution of TS for achieving statistically reliable profile evolution for such a perturbative transport study.

Interestingly, the super-resolution TS has once again enabled the inspection of rapid profile evolution during perturbative RMP, providing the first experimental evidence of the RMP-induced island effect. Figure 4(b-i) illustrates the recovery of temperature and density pedestals within 10 ms after deactivating the RMP, as captured through numerical modeling (see Figure 4(b-e)) and super-resolution TS (see Figure 4(f-i)). Here, the Chebyshev filter is used to derive a statistically reliable time trace of the profile, leveraging the enhanced temporal resolution. The simulations reveal that the recovery of temperature and density pedestals begins at the top and foot, coinciding with the disappearance of islands at rational surfaces with safety factors  $q=11/3, 13/3$ , and  $14/3$ . As depicted in Figure 4(d) and Figure 4(e), the profile gradient recovers at these island locations, enhancing the overall profile. This recovery behavior is also mirrored in the super-resolution TS measurements. For instance, the measured electron temperature pedestal shows recovery at both the top and foot through an increasing gradient, displaying qualitative alignment with the simulation results. However, some discrepancies are noted, particularly in the density evolution at the pedestal foot in the super-resolution TS, even though its gradient remains consistent with the modeling. These quantitative differences may stem from the TS's limited spatial resolution and the modeling assumptions, such as fixed boundary conditions [21]. Nevertheless, the gradient evolution directly indicates a change in transport due to the RMP-induced islands during this perturbative profile evolution, highlighting that the super-resolution TS successfully reveals the experimental island effect. This provides the first diagnostic evidence of profile flattening at magnetic islands, a key mechanism of RMP-induced pedestal degradation. This successful application of super-resolution TS underscores its potential to reveal new physics beyond the limitations of conventional diagnostic techniques.

## 5 Discussion and conclusion

This study introduces a transformative approach in the field of signal processing and diagnostics through the development of a multimodal neural network model, Diag2Diag, which significantly enhances temporal resolution. By leveraging the intrinsic correlations among various diagnostics, we have demonstrated the potential to increase the temporal resolution of the Thomson Scattering (TS) diagnostic in fusion plasma from a standard 0.2 kHz to an unprecedented 500 kHz. This improvement has unlocked new potentials in analyzing fast transient phenomena in plasma, such as the ELMs and the effects

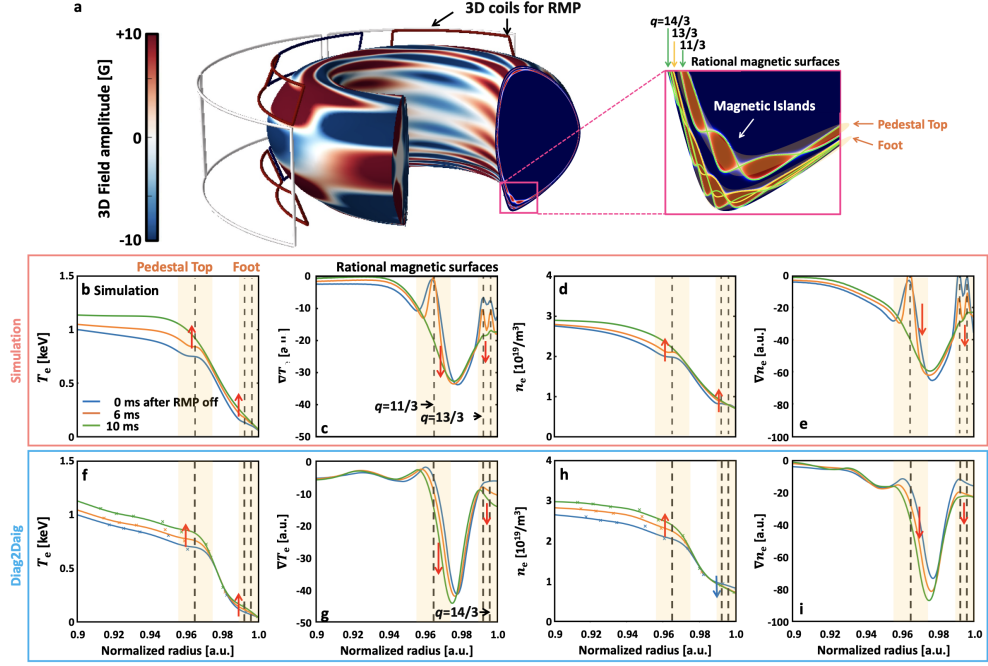


**Fig. 4:** Structure of 3D coils and islands by perturbed field (a), and the evidence in TM1 simulation (b-e) and super-resolution TS diagnostic (f-i) for RMP-induced island mechanism on the plasma boundary in DIII-D shot number 157545.

of RMPs on pedestal degradation, which were previously blurred or missed in lower resolution data. The ability to inspect these dynamics in greater detail provides new insights into plasma behavior, particularly in conditions where key physics is hidden in the milliseconds. This enhancement is not merely a technical improvement but a crucial enabler for deeper insights into plasma behaviors that are pivotal for advancing Fusion Power Plants (FPP).

The implications of this work extend well beyond the immediate application to FPP. The super-resolution capabilities developed here can significantly impact areas such as laser fusion data analysis, accelerator data analysis, and molecular dynamics research. In these fields, similar challenges exist where the time resolution of diagnostics is inadequate to capture fast phenomena effectively. By applying our model, researchers can potentially uncover new physical phenomena or confirm theoretical predictions that were previously unverifiable through experiments due to resolution constraints.

Furthermore, the model's ability to reconstruct and predict diagnostics from multimodal inputs opens new avenues for cost-effective and less hardware-dependent diagnostic systems. This is particularly beneficial for experimental setups where space and resources are limited, such as in smaller fusion test facilities or in environments where installing multiple high-resolution diagnostics is impractical.

In conclusion, the Diag2Diag model not only addresses a critical need within the fusion community but also sets a precedent for the broader application of AI and

machine learning in physical sciences. By pushing the boundaries of what can be observed and measured, this work contributes to the foundational technologies necessary for the realization of fusion energy and advances our understanding of complex physical systems across various scientific domains.

## 6 Methods

### 6.1 Diagnostic details for ELM

In order to let fusion energy be a viable energy source, it must achieve significant fusion gain through continuous fusion reactions. A prominent method to reach this objective is operating a tokamak in high confinement mode (H-mode), which has a narrow edge transport barrier, also known as the pedestal. This feature significantly boosts plasma confinement within the reactor, enhancing fusion power and efficiency. However, operating in H-mode introduces a steep pressure gradient at the pedestal, leading to substantial operational risks. This gradient drives hazardous edge energy bursts due to a plasma instability known as [ELMs](#). These bursts lead to sudden drops in the energy at the pedestal, causing severe, transient heat fluxes on the reactor walls. This results in damaging material, potential surface erosion and melting, with heat energy reaching approximately  $20 \text{ MJ m}^{-2}$ , which is an unacceptable level for fusion reactors. From [ITER](#), future machines will not allow even the first [ELM](#). Therefore, to advance tokamak designs toward practical application in fusion energy, it is crucial to develop dependable methods to consistently suppress these edge burst events.

A limitation of some diagnostics, such as [TS](#) is the low temporal resolution of only 200 Hz, which does not allow for detecting and tracking fast events like [ELM](#) ( $\leq 1 \text{ ms}$ ). Figure 5 shows an example of missing [ELM](#) in a discharge, due to the low temporal resolution of [TS](#). Nevertheless, it is still important to detect such events reliably, as they can have a strong impact on plasma behavior. In DIII-D there is a specific operational method to increase the sampling rate of [TS](#) up to 10 kHz (also known as “bunch mode”) [22]. However due to its limitations including high energy consumption, equipment stress, heat generation, complex data analysis, and limited measurement repetition, bunch mode is not effective at the pedestal and is typically reserved for specific experimental runs or particular phases of reactor operation where high-resolution temporal data is crucial.

On the other hand, diagnostics like [Interferometer](#), [ECE](#), have much higher temporal resolution with sampling frequencies around MHz, which allows for a much more detailed analysis of the plasma. However, these diagnostics have different characteristics compared to [TS](#). While [TS](#) offers detailed insights into both electron density and temperature with high accuracy, it requires complex setups and is usually more resource-intensive. A [Interferometer](#) provides a more straightforward approach to measuring electron density, excelling in situations that require rapid response and continuous monitoring. Furthermore, [ECE](#) and [TS](#) are both pivotal diagnostic tools used in tokamaks for measuring electron temperature, yet they operate on distinctly different principles and offer unique advantages. [ECE](#) utilizes the natural microwave emissions from electrons gyrating around magnetic field lines to provide excellent temporal resolution, allowing for the monitoring of rapid plasma changes and instabilities, though

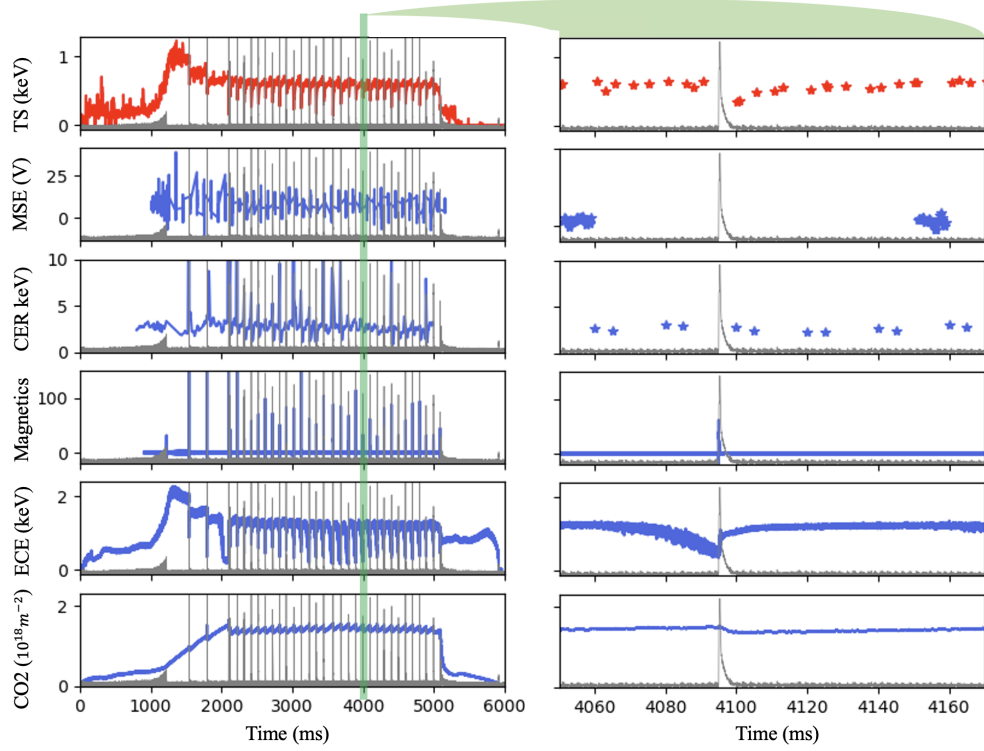


**Fig. 5:** (Left) Example of **TS** signal for DIII-D discharge 174823, in red, along with the  $D_\alpha$  measurements, in gray, as an indicator of **ELM**, and a collection of other diagnostics that will be used to increase the resolution of **TS**. (Right) The same data as left but zoomed in to show the sampling points of the diagnostics around one example of **ELM** event. Due to the low sampling rate, this **ELM** is not observed by **TS**. However, thanks to their high temporal resolution, diagnostics including **ECE**, **Interferometer**, and **Magnetics** capture that.

its effectiveness can be limited by variations in magnetic field strength. On the other hand, **TS** involves firing a laser into the plasma and analyzing the scattered light, which provides robust, absolute measurements of both electron temperature and density with less susceptibility to magnetic influences. While **ECE** excels in continuous data collection and fine temporal analysis, **TS** offers superior spatial resolution and is less dependent on external conditions, making it invaluable for comprehensive, though typically less frequent, plasma evaluations. If it would be possible to find a correlation between those high-resolution diagnostics and **TS**, this would be useful for developing new physical analyses.

## 6.2 Data acquisition

For this experiment, we used discharges from the DIII-D tokamak that include all data from the key diagnostics of interest (CER, Interferometer, ECE, MSE, and TS). We randomly selected 4000 discharges recorded between the years 2017 and 2022 to ensure a diverse and representative dataset. The diagnostic data was collected using the DIII-D MDSplus [23] and PTDATA [24] systems. These diagnostics are generally provided as time-series data streams with varying sampling frequencies, ranging from 200 Hz for TS up to 1.66 MHz for Interferometer. The specific pre-processing steps applied to the data for the different experiments conducted in this study are detailed in the following sections.

## 6.3 Feature extraction

For the spectrogram experiments, we consider the Interferometer and ECE diagnostics. We compute logarithmic magnitude spectrogram from raw series using hamming windows of 1ms with 0.5ms overlap. Given the noisy nature of the ECE signals and after rescaling the spectrograms to the range of [0,1], the spectrograms are enhanced using a pipeline of image processing filters that includes

- Quantile Filtering with a threshold of 0.9,
- Gaussian Blur Filtering on patches of size 31x3,
- Subtracting average per frequency bin

The starting point is the raw time-series of the diagnostics, i.e., ECE with 40 channels at 500 kHz, and Interferometer with 4 channels at 1.66 MHz. For each channel, spectrograms were computed independently. The ECE spectrograms were computed with a window size of 512 samples, and with a hop size of 256 samples. The Interferometer spectrograms were computed with a window size of 1536 samples, and with a hop size of 768 samples. In this way, it was ensured that the different magnitude spectrograms were aligned in time. Afterwards, the linear magnitudes are converted to a logarithmic scale, and the spectrograms were clipped and rescaled to the range of [0, 1].

We used the ECE spectrograms as inputs to our model. Since we treated every ECE channel independently during feature extraction, we obtained one spectrogram per channel, resulting in 40 input spectrograms (one per ECE channel). Since our model is designed to estimate the Interferometer spectrograms, it predicts four output spectrogram channels corresponding to the four Interferometer interferometer channels.

For the time-series models, the different diagnostic measurements have varying sampling rates, and some are even non-uniformly sampled in time. Since the aim of time-series data analysis was to increase the resolution of TS, we used its timestamps as a reference and aligned all diagnostic modalities to TS by matching their most recent measured samples in time. This resulted in an amount of 135 233 training, 22 084 validation, and 18 721 test samples.

For Interferometer and ECE, we also included the first and second temporal derivatives. Therefore, we smoothed the signals with a moving average window of 1 ms (1660 Interferometer samples and 500 ECE samples), and then computed the first and second

temporal derivatives of the smoothed signal also with a window of 1 ms. In this way, we can consider a temporal context of 4 ms.

The diagnostics [CER](#) and [MSE](#) have a low temporal resolution, i.e., sampling frequencies of 200 Hz and 4 kHz, respectively. In this paper, we assume that they evolve only slowly in time. For the upsampling experiments, we thus pad these diagnostics after a measured sample with constant values until the next measured sample arrived.

The diagnostics ([CER](#), [Interferometer](#), [ECE](#), and [MSE](#)) together with the derivatives of [Interferometer](#) (4 channels  $\rightarrow$  12 dimensions including derivatives) and [ECE](#) (42 channels  $\rightarrow$  126 dimensions) lead to an input size of 192. From there, we map to [TS](#) with 288 dimensions for plasma density and temperature.

## 6.4 Spectrogram model development

The resulting multi-channel [ECE](#) spectrograms were used as the input to a [CNN](#), and the multi-channel [Interferometer](#) spectrograms were used as the target outputs. We optimized all important hyper-parameters based on the  $R^2$  score to maximize the similarity between the ground truth and the estimated outputs on the training and validation sets.

We developed a [CNN](#) model for the task of predicting spectrograms. This model was trained to estimate [Interferometer](#) spectrograms based on input from [ECE](#) spectrograms. The optimization process of the model involved several key steps:

- The model underwent training for up to 500 epochs.
- We implemented early stopping with a patience threshold of 20 epochs, during which we monitored the validation loss for any improvements.
- The AdamW optimizer [25], known for decoupling weight decay from the learning rate, was utilized to minimize the  $\mathcal{L}_1$  loss function.
- We conducted a comprehensive hyper-parameter optimization through a randomized search across 1000 iterations for all hyper-parameters listed in Table 1.

The exact search space of the hyper-parameters and their optimized values obtained from the randomized search are summarized in Table 1.

**Table 1:** Optimized hyperparameters for the spectrogram prediction [CNN](#) model.

Hyper-parameter	Search space	Optimized value
Batch size	1 to 8, random integers	2
Kernel size	3 to 15 odd integers	7
Learning rate	$1 \times 10^{-5}$ to 1 log uniform	$0.482 \times 10^{-3}$
Final $R^2$ score	–	0.87

To reduce the amount of training time, we randomly selected 518 discharges from the entire dataset to conduct the hyperparameter optimization. The model with the

best performing hyperparameter setting (achieving an  $R^2$  score of 0.87 on the validation set) was then re-trained on all 5000 available discharges.

The best-performing model is a [CNN](#) that transforms the [ECE](#) spectrograms with 40 channels subsequently to 32, 16 and 8 feature maps and finally to the [Interferometer](#) spectrograms with 4 channels. For each feature map, 2D filter kernels with a size of  $7 \times 7$  are used. Batch normalization was used separately for each channel, and parametric ReLU activation functions were used after each batch normalization layer. The model had in total 95 823 trainable parameters (i.e., filter kernels for each feature map, batch normalization parameters, and negative slope of the parametric ReLU activation function).

## 6.5 Time-series model development

For the time-series prediction task, we employed a [MLP](#) model. The input data to the [MLP](#) comprised the [CER](#), [Interferometer](#), [ECE](#), [MSE](#), and magnetic diagnostics, along with the first and second temporal derivatives of the [Interferometer](#) and [ECE](#) signals, resulting in a total input size of 236 dimensions. The target output was the [TS](#) diagnostic data, which had 80 dimensions representing electron temperature and density across various spatial locations. The target data were augmented by factor 2 by using the upper and lower intervals of each sample as additional targets.

The [MLP](#) model was trained for a maximum of 500 epochs, with an early stopping mechanism implemented to halt the training process if the validation loss did not improve for 20 consecutive epochs. The AdamW optimizer [25] was employed to minimize the  $\mathcal{L}_1$  loss function during training.

As for the spectrogram model, a comprehensive hyperparameter optimization was undertaken using a randomized search approach spanning 2000 iterations. The hyperparameters jointly optimized included the batch size, hidden layer size, dropout rate, and learning rate.

Table 2 summarizes the optimized hyperparameter values obtained from the randomized search process.

**Table 2:** Optimized hyperparameters for the time-series [MLP](#) model.

Hyper-parameter	Search space	Optimized value
Batch size	1 to 2048, powers of 2	1024
Hidden layer size	192 to 2048 integers	952
Dropout	0 to 1 uniform	0.076
Learning rate	$1 \times 10^{-5}$ to 1 log uniform	$1.998 \times 10^{-3}$
Final $R^2$ score	–	0.92



## 6.6 Related works

In recent years different kinds of a **NN** have been used for upsampling visual data [26–30] and for radar data [31–34]. These approaches are typically some kind of non-linear interpolation to add frames between existing video frames. More examples for **ML**-based upsampling were proposed for medical data [35] and for audio data [36–39]. Similar to the video upsampling approaches, these approaches are some kind of non-linear interpolation as well. In [40], an alternative to interpolation is suggested to estimate missing data in temporal data streams. It is kind of a multimodal approach, because it fuses different kinds of information. However, the algorithm is limited towards estimating missing data or dealing with irregularly sampled data. Approaches like these work well for enhancing existing sequences, which are quasi-stationary in a way such that consecutive frames or samples do not change very fast.

However, in nuclear fusion, many spurious events like **ELM** can happen between two **TS** samples. By interpolating between consecutive **TS** samples, regardless of linearly or non-linearly, it is likely that we would miss such spurious events. In this paper, we thus develop a novel method to generate additional **TS** samples based on other diagnostics. This is roughly inspired by other multimodal **ML** approaches, such as [41], where it was proposed to fuse Radar and camera data for an enhanced distance estimation. This is a multimodal approach and thus related to our approach, or [42], where machine learning was used to reveal the control mechanics of an insect wing hinge. This was also a multimodal approach in a way that the **ML** algorithm received different features recorded from flying insects. However, similar to the other approaches, no attempts to upsampling or estimating missing/in-between data are made.

**Acknowledgements.** This material is based upon work supported by the U.S. Department of Energy, Office of Science, Office of Fusion Energy Sciences, using the National Fusion Facility, a DOE Office of Science user facility, under Award DE-FC02-04ER54698. In addition this material was supported by the U.S. Department of Energy, under Awards DE- SC0015480, DE-SC0024527.

Disclaimer: This report was prepared as an account of work sponsored by an agency of the United States Government. Neither the United States Government nor any agency thereof, nor any of their employees, makes any warranty, express or implied, or assumes any legal liability or responsibility for the accuracy, completeness, or usefulness of any information, apparatus, product, or process disclosed, or represents that its use would not infringe privately owned rights. Reference herein to any specific commercial product, process, or service by trade name, trademark, manufacturer, or otherwise does not necessarily constitute or imply its endorsement, recommendation, or favoring by the United States Government or any agency thereof. The views and opinions of authors expressed herein do not necessarily state or reflect those of the United States Government or any agency thereof.

## References

- [1] Seo, J., Kim, S., Jalalvand, A., Conlin, R., Rothstein, A., Abbate, J., Erickson, K., Wai, J., Shousha, R., Kolemen, E.: Avoiding fusion plasma tearing instability

- with deep reinforcement learning. *Nature* **626**(8000), 746–751 (2024) <https://doi.org/10.1038/s41586-024-07024-9>
- [2] Kim, S.K., Shousha, R., Yang, S.M., Hu, Q., Hahn, S.H., Jalalvand, A., Park, J.-K., Logan, N.C., Nelson, A.O., Na, Y.-S., Nazikian, R., Wilcox, R., Hong, R., Rhodes, T., Paz-Soldan, C., Jeon, Y.M., Kim, M.W., Ko, W.H., Lee, J.H., Battey, A., Yu, G., Bortolon, A., Snipes, J., Kolemen, E.: Highest fusion performance without harmful edge energy bursts in tokamak. *Nature Communications* **15**(1), 3990 (2024) <https://doi.org/10.1038/s41467-024-48415-w> . Accessed 2024-05-13
  - [3] Chouchene, S., Brochard, F., Lemoine, N., Cavalier, J., Desecures, M., Weinzettl, V.: Mutual interactions between plasma filaments in a tokamak evidenced by fast imaging and machine learning. *Phys. Rev. E* **109**, 045201 (2024) <https://doi.org/10.1103/PhysRevE.109.045201>
  - [4] Degraeve, J., Felici, F., Buchli, J., Neunert, M., Tracey, B., Carpanese, F., Ewalds, T., Hafner, R., Abdolmaleki, A., Casas, D., Donner, C., Fritz, L., Galperti, C., Huber, A., Keeling, J., Tsimpoukelli, M., Kay, J., Merle, A., Moret, J.-M., Noury, S., Pesamosca, F., Pfau, D., Sauter, O., Sommariva, C., Coda, S., Duval, B., Fasoli, A., Kohli, P., Kavukcuoglu, K., Hassabis, D., Riedmiller, M.: Magnetic control of tokamak plasmas through deep reinforcement learning. *Nature* **602**(7897), 414–419 (2022) <https://doi.org/10.1038/s41586-021-04301-9>
  - [5] Ding, S., Garofalo, A.M., Wang, H.Q., Weisberg, D.B., Li, Z.Y., Jian, X., Eldon, D., Victor, B.S., Marinoni, A., Hu, Q.M., Carvalho, I.S., Odstrčil, T., Wang, L., Hyatt, A.W., Osborne, T.H., Gong, X.Z., Qian, J.P., Huang, J., McClenaghan, J., Holcomb, C.T., Hanson, J.M.: A high-density and high-confinement tokamak plasma regime for fusion energy. *Nature* (2024) <https://doi.org/10.1038/s41586-024-07313-3>
  - [6] Boivin, R.L., Luxon, J.L., Austin, M.E., Brooks, N.H., Burrell, K.H., Doyle, E.J., Fenstermacher, M.E., Gray, D.S., Groth, M., Hsieh, C.-L., Jayakumar, R.J., Lasnier, C.J., Leonard, A.W., McKee, G.R., Moyer, R.A., Rhodes, T.L., Rost, J.C., Rudakov, D.L., Schaffer, M.J., Strait, E.J., Thomas, D.M., Van Zeeland, M., Watkins, J.G., Watson, G.W., Wong, C.P.C.: Diii-d diagnostic systems. *Fusion Science and Technology* **48**(2), 834–851 (2005) <https://doi.org/10.13182/FST05-A1043>
  - [7] Haskey, S.R., Grierson, B.A., Stagner, L., Chrystal, C., Bortolon, A., Laggner, F.M.: Details of the neutral energy distribution and ionization source using spectrally resolved Balmer-alpha measurements on DIII-D. *Review of Scientific Instruments* **93**(10), 103504 (2022) <https://doi.org/10.1063/5.0101854> [https://pubs.aip.org/aip/rsi/article-pdf/doi/10.1063/5.0101854/16594766/103504.1\\_online.pdf](https://pubs.aip.org/aip/rsi/article-pdf/doi/10.1063/5.0101854/16594766/103504.1_online.pdf)
  - [8] Strait, E.J.: Magnetic diagnostic system of the DIII-D tokamak. *Review of Scientific Instruments* **77**(2), 023502 (2006) <https://doi.org/10.1063/1.2202000>

[//doi.org/10.1063/1.2166493](https://doi.org/10.1063/1.2166493) [https://pubs.aip.org/aip/rsi/article-pdf/doi/10.1063/1.2166493/16053320/023502.1\\_online.pdf](https://pubs.aip.org/aip/rsi/article-pdf/doi/10.1063/1.2166493/16053320/023502.1_online.pdf)

- [9] Holcomb, C.T., Makowski, M.A., Jayakumar, R.J., Allen, S.A., Ellis, R.M., Geer, R., Behne, D., Morris, K.L., Seppala, L.G., Moller, J.M.: Motional Stark effect diagnostic expansion on DIII-D for enhanced current and Er profile measurements. *Review of Scientific Instruments* **77**(10), 10–506 (2006) <https://doi.org/10.1063/1.2235812> [https://pubs.aip.org/aip/rsi/article-pdf/doi/10.1063/1.2235812/11170995/10e506.1\\_online.pdf](https://pubs.aip.org/aip/rsi/article-pdf/doi/10.1063/1.2235812/11170995/10e506.1_online.pdf)
- [10] Ponce-Marquez, D.M., Bray, B.D., Deterly, T.M., Liu, C., Eldon, D.: Thomson scattering diagnostic upgrade on DIII-Da). *Review of Scientific Instruments* **81**(10), 10–525 (2010) <https://doi.org/10.1063/1.3495759> [https://pubs.aip.org/aip/rsi/article-pdf/doi/10.1063/1.3495759/13981451/10d525.1\\_online.pdf](https://pubs.aip.org/aip/rsi/article-pdf/doi/10.1063/1.3495759/13981451/10d525.1_online.pdf)
- [11] Joung, S., Smith, D.R., McKee, G., Yan, Z., Gill, K., Zimmerman, J., Geiger, B., Coffee, R., O’Shea, F.H., Jalalvand, A., Kolemen, E.: Tokamak edge localized mode onset prediction with deep neural network and pedestal turbulence. *Nuclear Fusion* **64**(6), 066038 (2024) <https://doi.org/10.1088/1741-4326/ad43fb>
- [12] Garcia, A.V., Jalalvand, A., Steiner, P., Rothstein, A., Van Zeeland, M., Heidbrink, W.W., Kolemen, E.: Comparison of machine learning systems trained to detect alfvén eigenmodes using the co2 interferometer on diii-d. *Nuclear Fusion* **63**(12), 126039 (2023) <https://doi.org/10.1088/1741-4326/acfe8b>
- [13] Nelson, A.O., Xing, Z.A., Izacard, O., Laggner, F.M., Kolemen, E.: Interpretative sol modeling throughout multiple elm cycles in diii-d. *Nuclear Materials and Energy* **26**, 100883 (2021) <https://doi.org/10.1016/j.nme.2020.100883>
- [14] Nazikian, R., Hu, Q., Ashourvan, A., Eldon, D., Evans, T.E., Grierson, B.A., Logan, N.C., Orlov, D.M., Park, J.-K., Paz-Soldan, C., Poli, F.M., Yu, Q.: Pedestal collapse by resonant magnetic perturbations. *Nuclear Fusion* **61**(4), 044001 (2021) <https://doi.org/10.1088/1741-4326/abd863>
- [15] Evans, T.E., Moyer, R.A., Burrell, K.H., Fenstermacher, M.E., Joseph, I., Leonard, A.W., Osborne, T.H., Porter, G.D., Schaffer, M.J., Snyder, P.B., Thomas, P.R., Watkins, J.G., West, W.P.: Edge stability and transport control with resonant magnetic perturbations in collisionless tokamak plasmas. *Nature Physics*, vol. 2, no. 6, June 1, 2006, pp. 419–423 **2**(6) (2006) <https://doi.org/10.1038/nphys312>
- [16] Hu, Q.M., Nazikian, R., Grierson, B.A., Logan, N.C., Park, J.-K., Paz-Soldan, C., Yu, Q.: The density dependence of edge-localized-mode suppression and pump-out by resonant magnetic perturbations in the DIII-D tokamak. *Physics of Plasmas* **26**(12), 120702 (2019) <https://doi.org/10.1063/1.5134767> [https://pubs.aip.org/aip/pop/article-pdf/doi/10.1063/1.5134767/13931866/120702.1\\_online.pdf](https://pubs.aip.org/aip/pop/article-pdf/doi/10.1063/1.5134767/13931866/120702.1_online.pdf)

- [17] Nazikian, R., Kirk, A., Suttrop, W., Cavedon, M., Grierson, B., Evans, T.E.: First observation of elm suppression by magnetic perturbations in asdex upgrade in a shape-matching identity experiment with diii-d. In: 26th IAEA Fusion Energy Conference (FEC 2016). IAEA, ??? (2016). <https://hdl.handle.net/11858/00-001M-0000-002C-A0F9-B>
- [18] Fitzpatrick, R.: Theory of edge localized mode suppression by static resonant magnetic perturbations in the DIII-D tokamak. *Physics of Plasmas* **27**(4), 042506 (2020) <https://doi.org/10.1063/5.0003117> [https://pubs.aip.org/aip/pop/article-pdf/doi/10.1063/5.0003117/19762313/042506\\_1\\_online.pdf](https://pubs.aip.org/aip/pop/article-pdf/doi/10.1063/5.0003117/19762313/042506_1_online.pdf)
- [19] Hu, Q.M., Nazikian, R., Grierson, B.A., Logan, N.C., Orlov, D.M., Paz-Soldan, C., Yu, Q.: Wide operational windows of edge-localized mode suppression by resonant magnetic perturbations in the diii-d tokamak. *Phys. Rev. Lett.* **125**, 045001 (2020) <https://doi.org/10.1103/PhysRevLett.125.045001>
- [20] Hu, Q.M., Park, J.-K., Logan, N.C., Yang, S.M., Grierson, B.A., Nazikian, R., Yu, Q.: Nonlinear two-fluid modeling of plasma response to rmeps for the elm control in the iter baseline. *Nuclear Fusion* **61**(10), 106006 (2021) <https://doi.org/10.1088/1741-4326/ac1d85>
- [21] Yu, Q., Strumberger, E., Igochine, V., Lackner, K., Laqua, H.P., Zanini, M., Braune, H., Hirsch, M., Höfel, U., Marsen, S., Stange, T., Wolf, R.C., Günter, S., Wendelstein 7-X Team: Numerical modeling of the electron temperature crashes observed in wendelstein 7-x stellarator experiments. *Nuclear Fusion* **60**(7), 076024 (2020) <https://doi.org/10.1088/1741-4326/ab9258>
- [22] HE, Z., SMITH, C., ZHANG, Z., BIEWER, T.M., JIANG, N., HSU, P.S., ROY, S.: Pulse-burst laser-based 10 khz thomson scattering measurements. *Plasma Science and Technology* **21**(10), 105603 (2019) <https://doi.org/10.1088/2058-6272/ab2e30>
- [23] Fredian, T.W., Stillerman, J.A.: Mdsplus. current developments and future directions. *Fusion Engineering and Design* **60**(3), 229–233 (2002) [https://doi.org/10.1016/S0920-3796\(02\)00013-3](https://doi.org/10.1016/S0920-3796(02)00013-3)
- [24] Schissel, D., McHarg Jr, B.: Data analysis infrastructure at the diii-d national fusion facility. General Atomics report No. GA-A23474 (2000)
- [25] Loshchilov, I., Hutter, F.: Decoupled weight decay regularization. In: International Conference on Learning Representations (2019). <https://openreview.net/forum?id=Bkg6RiCqY7>
- [26] Wang, Z., Lin, S., Teng-Levy, M., Chu, P., Wolfe, B.T., Wong, C.-S., Campbell, C.S., Yue, X., Zhang, L., Aberle, D., Alvarez, M.A., Broughton, D., Chen, R.T., Cheng, B., Chu, F., Fossum, E.R., Foster, M.A., Huang, C., Kilic, V., Krushelnick, K., Li, W., Loomis, E., au2, T.S.J., Sjue, S.K., Tomkins, C., Yarotski, D.A., Zhu, R.: Physics-informed Meta-instrument for eXperiments (PiMiX) with applications

to fusion energy (2024)

- [27] Jiang, H., Sun, D., Jampani, V., Yang, M.-H., Learned-Miller, E., Kautz, J.: Super slo-mo: High quality estimation of multiple intermediate frames for video interpolation. In: Proceedings of the IEEE Conference on Computer Vision and Pattern Recognition (CVPR) (2018)
- [28] Niklaus, S., Liu, F.: Context-aware synthesis for video frame interpolation. In: Proceedings of the IEEE Conference on Computer Vision and Pattern Recognition (CVPR) (2018)
- [29] Bao, W., Lai, W.-S., Ma, C., Zhang, X., Gao, Z., Yang, M.-H.: Depth-aware video frame interpolation. In: Proceedings of the IEEE/CVF Conference on Computer Vision and Pattern Recognition (CVPR) (2019)
- [30] Xue, T., Chen, B., Wu, J., Wei, D., Freeman, W.T.: Video enhancement with task-oriented flow. *International Journal of Computer Vision* **127**(8), 1106–1125 (2019) <https://doi.org/10.1007/s11263-018-01144-2>
- [31] Che, Z., Purushotham, S., Li, G., Jiang, B., Liu, Y.: Hierarchical deep generative models for multi-rate multivariate time series. In: Dy, J., Krause, A. (eds.) Proceedings of the 35th International Conference on Machine Learning. Proceedings of Machine Learning Research, vol. 80, pp. 784–793. PMLR, ??? (2018). <https://proceedings.mlr.press/v80/che18a.html>
- [32] Recla, M., Schmitt, M.: Deep-learning-based single-image height reconstruction from very-high-resolution sar intensity data. *ISPRS Journal of Photogrammetry and Remote Sensing* **183**, 496–509 (2022) <https://doi.org/10.1016/j.isprsjprs.2021.11.012>
- [33] Recla, M., Schmitt, M.: Improving deep learning-based height estimation from single sar images by injecting sensor parameters. In: IGARSS 2023 - 2023 IEEE International Geoscience and Remote Sensing Symposium, pp. 1806–1809 (2023). <https://doi.org/10.1109/IGARSS52108.2023.10282228>
- [34] Roßberg, T., Schmitt, M.: Temporal upsampling of ndvi time series by rnn-based fusion of sparse optical and dense sar-derived ndvi data. In: IGARSS 2023 - 2023 IEEE International Geoscience and Remote Sensing Symposium, pp. 5990–5993 (2023). <https://doi.org/10.1109/IGARSS52108.2023.10282861>
- [35] Bellos, D., Basham, M., Pridmore, T., French, A.P.: A convolutional neural network for fast upsampling of undersampled tomograms in x-ray ct time-series using a representative highly sampled tomogram. *Journal of Synchrotron Radiation* **26**(3), 839–853 (2019) <https://doi.org/10.1107/S1600577519003448>
- [36] Pascual, S., Bonafonte, A., Serrà, J.: Segan: Speech enhancement generative adversarial network. In: Proceedings of the Interspeech 2017, pp. 3642–3646 (2017).

<https://doi.org/10.21437/Interspeech.2017-1428>

- [37] Donahue, C., McAuley, J., Puckette, M.: Adversarial audio synthesis. In: International Conference on Learning Representations (2019). <https://openreview.net/forum?id=ByMVTsR5KQ>
- [38] Pandey, A., Wang, D.: Densely connected neural network with dilated convolutions for real-time speech enhancement in the time domain. In: ICASSP 2020 - 2020 IEEE International Conference on Acoustics, Speech and Signal Processing (ICASSP), pp. 6629–6633 (2020). <https://doi.org/10.1109/ICASSP40776.2020.9054536>
- [39] Kumar, K., Kumar, R., Boissiere, T., Gestin, L., Teoh, W.Z., Sotelo, J., Brébisson, A., Bengio, Y., Courville, A.C.: Melgan: Generative adversarial networks for conditional waveform synthesis. In: Wallach, H., Larochelle, H., Beygelzimer, A., Alché-Buc, F., Fox, E., Garnett, R. (eds.) *Advances in Neural Information Processing Systems*, vol. 32. Curran Associates, Inc., ??? (2019). [https://proceedings.neurips.cc/paper\\_files/paper/2019/file/6804c9bca0a615bdb9374d00a9fcba59-Paper.pdf](https://proceedings.neurips.cc/paper_files/paper/2019/file/6804c9bca0a615bdb9374d00a9fcba59-Paper.pdf)
- [40] Yoon, J., Zame, W.R., Schaar, M.: Estimating missing data in temporal data streams using multi-directional recurrent neural networks. *IEEE Transactions on Biomedical Engineering* **66**(5), 1477–1490 (2019) <https://doi.org/10.1109/TBME.2018.2874712>
- [41] Li, Y., Wang, Y., Meng, C., Duan, Y., Ji, J., Zhang, Y., Zhang, Y.: Farfusion: A practical roadside radar-camera fusion system for far-range perception. *IEEE Robotics and Automation Letters*, 1–8 (2024) <https://doi.org/10.1109/LRA.2024.3387700>
- [42] Melis, J.M., Siwanowicz, I., Dickinson, M.H.: Machine learning reveals the control mechanics of an insect wing hinge. *Nature* **628**(8009), 795–803 (2024) <https://doi.org/10.1038/s41586-024-07293-4>